Multiscale Phase Inversion of Seismic Marine Data

Lei Fu
King Abdullah University of Science and Technology (KAUST), Thuwal 23955-6900, Kingdom of Saudi Arabia.

SUMMARY

We test the feasibility of applying multiscale phase inversion (MPI) to seismic marine data. To avoid cycle-skipping, the multiscale strategy temporally integrates the traces several times , i.e. high-order integration, to produce low-boost seismograms that are used as input data for the initial iterations of MPI. As the iterations proceed, higher frequencies in the data are boosted by using integrated traces of lower order as the input data. Results with synthetic data and field data from the Gulf of Mexico produce robust and accurate results if the model does not contain strong velocity contrasts such as salt-sediment interfaces.

INTRODUCTION

One of the most significant problems with full waveform inversion (FWI) is the cycle-skipping problem (Virieux and Operto, 2009; Warner et al., 2013; Warner and Guasch, 2014), where an iterative solution gets stuck in a local minimum. Another problem is that the amplitudes of the predicted traces do not fully match those of the observed data because all of the actual physics is not used in computing the predicted traces. To mitigate both problems, Sun and Schuster (1993) proposed a multiscale phase inversion (MPI) method. To avoid cycle-skipping, the multiscale strategy temporally integrates the traces several times to produce low-boost seismograms that are used as input data for the initial iterations of MPI. To avoid the necessity of exactly predicting amplitudes, only the phase of the seismic data is predicted and the amplitude information is largely ignored. The penalty in not matching amplitudes is a moderate loss in resolution in the velocity tomogram. Sun and Schuster (1993) demonstrated the feasibility of this method by applying it to synthetic crosswell data. We now test the MPI strategy on both synthetic data and field data recorded in a marine seismic sruvey. The next section describes the theory of MPI, which is then followed by the numerical results section. Both synthetic data and field data are inverted with the MPI strategy for sediments with moderate velocity contrasts. The final section presents the summary.

THEORY

For phase inversion, we replace the magnitude spectrum of a calculated trace with the magnitude spectrum of the corresponding observed trace so that the amplitude strengths of two traces are equalized. The predicted and observe traces are Fourier transformed to obtain the magnitude A and phase ϕ spectra, where

$$\mathscr{F}\left[p(\mathbf{g},t;\mathbf{s})_{cal}\right] = A(\mathbf{g},\omega;\mathbf{s})_{cal}\, e^{i\phi(\mathbf{g},\omega;\mathbf{s})_{cal}}, \quad (1)$$

$$\mathscr{F}\left[p(\mathbf{g},t;\mathbf{s})_{obs}\right] = A(\mathbf{g},\omega;\mathbf{s})_{obs}\, e^{i\phi(\mathbf{g},\omega;\mathbf{s})_{obs}}. \quad (2)$$

Here, $\mathbf{s}$ is the location of the source, and $\mathbf{g}$ is the location of the geophone for a monochromatic source at frequency ω. The modified traces $\bar{p}(\mathbf{g},t;\mathbf{s})_{cal}$ are obtained by replacing $A(\mathbf{g},\omega;\mathbf{s})_{cal}$ with $A(\mathbf{g},\omega;\mathbf{s})_{obs}$ and performing the inverse Fourier transform,

$$\bar{p}(\mathbf{g},t;\mathbf{s})_{cal} = \mathscr{F}^{-1}\left\{L(\omega)A(\mathbf{g},\omega;\mathbf{s})_{new} e^{i\phi(\mathbf{g},\omega;\mathbf{s})_{cal}}\right\}, \quad (3)$$

$$\bar{p}(\mathbf{g},t;\mathbf{s})_{obs} = \mathscr{F}^{-1}\left\{L(\omega)A(\mathbf{g},\omega;\mathbf{s})_{obs} e^{i\phi(\mathbf{g},\omega;\mathbf{s})_{obs}}\right\}, \quad (4)$$

where $A(\mathbf{g},\omega;\mathbf{s})_{new} = A(\mathbf{g},\omega;\mathbf{s})_{obs}$ and $L(\omega)$ is a low-pass filter applied to data.

Misfit function. The modified predicted and observed traces are time-integrated and their residual are used for the MPI misfit function,

$$\varepsilon^{mpi} = \sum_{\mathbf{s},\mathbf{g}} \int dt \left[I^n \bar{p}(\mathbf{g},t;\mathbf{s})_{cal} - I^n \bar{p}(\mathbf{g},t;\mathbf{s})_{obs}\right]^2, \quad (5)$$

where I^n is an integration operator $I \equiv \int dt$ performed n times, and $\bar{p}(\mathbf{g},t;\mathbf{s})_{cal}$ and $\bar{p}(\mathbf{g},t;\mathbf{s})_{obs}$ are the modified traces in equations (3) and (4). If we set $A(\mathbf{g},\omega;\mathbf{s})_{new} = A(\mathbf{g},\omega;\mathbf{s})_{cal}$ in equation (3), then the MPI misfit function becomes that for full wave inversion, except that the traces have been modified by the filter $L(\omega)$ and integration operator.

Gradient. The gradient of MPI misfit function ε^{mpi} w.r.t. the velocity field $c(\mathbf{x})$

$$\begin{aligned}\gamma^{mpi}(\mathbf{x}) &= \frac{\partial \varepsilon^{mpi}}{\partial c(\mathbf{x})} \\ &= \frac{1}{c(\mathbf{x})^3} \sum_{\mathbf{s}} \int dt \left[I^n \dot{\bar{p}}(\mathbf{x},t;\mathbf{s})\right]\left[I^n \dot{\bar{p}}'(\mathbf{x},t;\mathbf{s})\right],\end{aligned} \quad (6)$$

where dot means time differentiation, $\bar{p}(\mathbf{x},t;\mathbf{s})$ is the pressure wavefield by the source at $\mathbf{s}$, and $\bar{p}'(\mathbf{x},t;\mathbf{s})$ is the wavefield computed by backprojecting the seismogram residual (Luo and Schuster, 1991) $\delta\bar{p}$,

$$\bar{p}'(\mathbf{x},t;\mathbf{s}) = \sum_r g(\mathbf{x},-t;\mathbf{g},0) * \delta\bar{p}, \quad (7)$$

with

$$\delta\bar{p} = \bar{p}(\mathbf{g},t;\mathbf{s})_{obs} - \bar{p}(\mathbf{g},t;\mathbf{s})_{cal}. \quad (8)$$

In theory, the integration operator I^n on the fields $\bar{p}$ and $\bar{p}'$ in equation 6 can be alternatively applied to source functions that generate them without changing the misfit gradient. For example, $I^n\dot{\bar{p}}(\mathbf{x},t;\mathbf{s})$ is equivalent to generating a wavefield using a source wavelet with I^{n-1} integrations.

For comparison, the traditional full wave inversion (FWI) gradient is

$$\gamma^{fwi}(\mathbf{x}) = \frac{\partial \varepsilon^{fwi}}{\partial c(\mathbf{x})} = \frac{1}{c(\mathbf{x})^3} \sum_{\mathbf{s}} \int dt \left[\dot{p}(\mathbf{x},t;\mathbf{s})\right] \left[\dot{p}'(\mathbf{x},t;\mathbf{s})\right], \tag{9}$$

where the FWI gradient is the dot product between the source forward modeled wavefield and the backprojected wavefield with the data residual $\delta p = p(\mathbf{g},t;\mathbf{s})_{obs} - p(\mathbf{g},t;\mathbf{s})_{cal}$.

Multiscale rrequency strategy. The data should be band-pass filtered into different frequency bands with different peak frequencies, and then the FWI or MPI method is used for low-frequency data at the early iterations and then high-frequency data at later iterations. A low-pass Wiener filter (Boonyasiriwat et al., 2009) can be computed by

$$L_{wiener}(\omega) = \frac{W_{target}(\omega) W^{\dagger}_{original}(\omega)}{|W_{original}(\omega)|^2 + \varepsilon^2}, \tag{10}$$

where $L_{wiener}(\omega)$ is the Wiener filter, $W_{original}(\omega)$ is the original wavelet, $W_{target}(\omega)$ is the target wavelet, $\dagger$ denotes complex conjugate, ω is the angular frequency, and ε is a damping factor to prevent numerical instability. One formula for choosing optimal frequency bands proposed by Sirgue and Pratt (2004) is

$$f_{n+1} = \frac{f_n}{\alpha_{min}}, \tag{11}$$

where f_n is the current frequency, f_{n+1} is the next frequency to be chosen, and $\alpha_{min} = z/\sqrt{h^2+z^2}$ is the parameter that depends on the maximum half offset h and the maximum depth z to be imaged.

NUMERICAL RESULTS

To demonstrate the effectiveness of MPI and its advantages, we invert one synthetic data from the Marmousi and marine data from the Gulf of Mexico. The modeling kernels are based on numerical solutions to the constant-density acoustic wave equation, while the observed input data are generated by solving the constant-density acoustic wave equation (Alford et al., 1974), visco-acoustic equation (Operto et al., 2007) or elastic equation (Levander, 1988) in the synthetic cases.

Marmousi Model

The Marmousi model (Figure 1a) is discretized into a 284 × 461 gridded velocity model with spacing of 10 m in both directions. There are 116 point sources spaced at an interval of 40 m on the free surface and 461 receivers separated by a 10 m interval along the free surface.

Acoustic Data

The original acoustic data are generated by solving the constant density acoustic equation with a 15-Hz Ricker wavelet. A common shot gather for the source at $(z,x) = (0,0)m$ is shown in Figure 2a. Different bandpass filters are applied to the original data, and the frequency multiscale strategy is used for both the FWI and MPI methods.

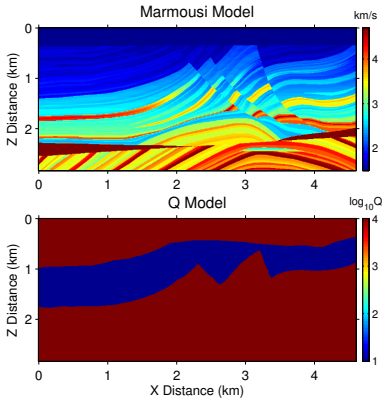

Figure 1: a) The Marmousi velocity model, b) the Q model used for generating visco-acoustic data.

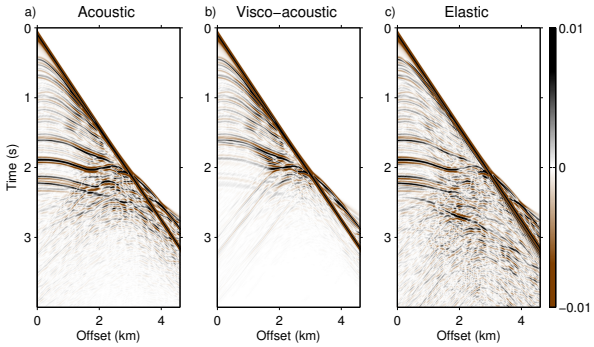

Figure 2: Synthetic seismic data, a) constant density acoustic data, b) visco-acoustic data, and c) elastic data, for the shot location at $x = 0$ km. All subplots have the same scale.

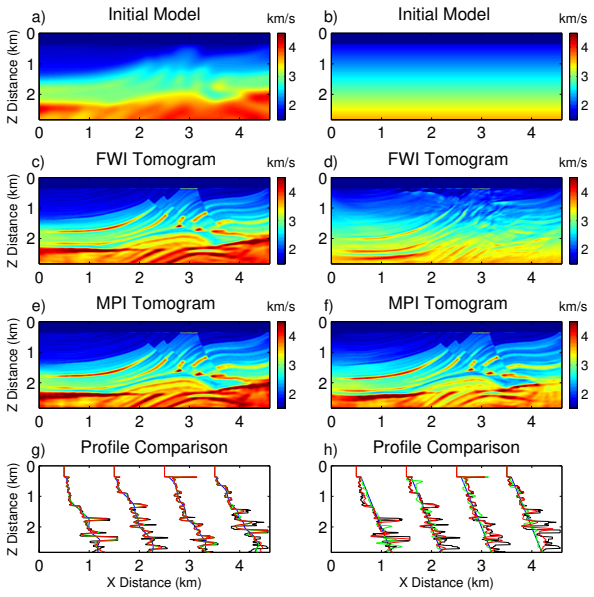

Figure 3: Inversion results for acoustic data. a) The smoothed initial velocity model with an average velocity error of 12%, c) FWI and e) MPI tomograms based on the initial model a), g) velocity profile comparison for true (black), initial (blue), FWI (green) and MPI (red) tomograms; b) the $v(z)$ initial velocity model with an average velocity error of 22%, d) FWI and f) MPI tomograms based on the initial model b), h) velocity profile comparison for true (black), initial (blue), FWI (green) and MPI (red) tomograms.

Figure 3a is the smoothed initial velocity model with an average velocity error of 12%, and Figure 3b is the $v(z)$ initial ve-

locity model with an average velocity error of 22%. The FWI and MPI tomograms with the smoothed initial model (Figure 3a) are shown in Figures 3c and 3e, respectively. The FWI and MPI tomograms with the $v(z)$ initial model (Figure 3b) are shown in Figures 3d and 3f, respectively. Figures 3g and 3h shows the velocity profile comparison for the true (black), initial (blue), FWI (green) and MPI (red) velocity models at different offsets. We can see that both the FWI and MPI tomograms have a good agreement with the true model when the initial model is not far away from the true model. However, when the initial model is far away from the true model, traditional FWI gets stuck in a local minima, while MPI provides an accurate tomogram. Thus, the MPI method has a more robust convergence than FWI for this model.

Visco-acoustic Data

We now use visco-acoustic data as input traces to the acoustic FWI and MPI algorithms. The goal is to test the sensitivity of each method to the unmodeled attenuation effects in the data. The visco-acoustic data are generated by solving visco-acoustic equations, where the source wavelet and acquisition geometry are the same as in the acoustic case. A pressure source is injected in the water, and the pressure field is recorded. The true v_p model is shown in Figure 1a and the Q model is shown in Figure 1b, where the minimum Q is 5. The visco-acoustic data for the shot location at $(z,x) = (0,0)m$ is shown in Figure 2b, where we can see that reflections are highly attenuated due to the highly attenuative medium. The acoustic FWI and MPI methods are applied to these synthetic visco-acoustic data, where the initial v_p model is shown in Figure 3a. The FWI and MPI tomograms are shown in Figures 4a and 4c, respectively, where the velocity profile comparison at different offsets are shown in Figure 4e. It is found that MPI is slightly more accurate than FWI.

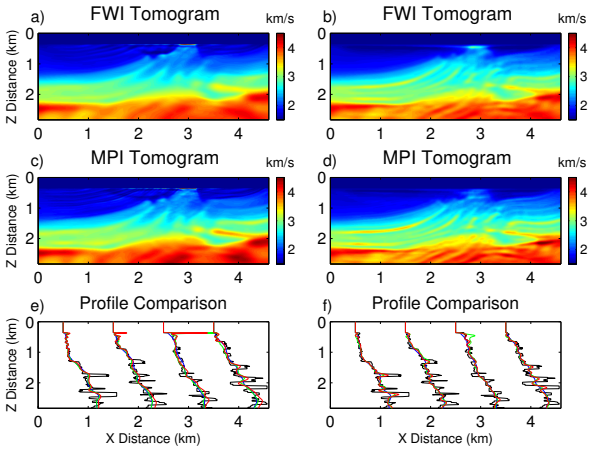

Figure 4: Inversion results for visco-acoustic and elastic data. a) FWI and, c) MPI tomograms, e) velocity profile comparison for true (black), initial (blue), FWI (green) and MPI (red) tomograms at different offsets for visco-acoustic data; b) FWI and d) MPI tomograms , f) velocity profile comparison for true (black), initial (blue), FWI (green) and MPI (red) tomograms at different offsets for elastic data.

Elastic Data

We now use elastic data as input traces to the acoustic FWI and MPI algorithms. The goal is to test the sensitivity of each method to the unmodeled elastic effects in the data. The elastic data are generated by solving the elastic wave equation, where the source wavelet and acquisition geometry are the same as in the acoustic case. The pressure is injected in the water and the pressure field is recorded as the negative of the average of the normal stresses. The true v_p model is shown in Figure 1a, the density is given by $\rho = 0.31 v_p^{0.25}$, and $v_s = v_p/\sqrt{3}$, except the shear velocity of the ocean water is set to 0 m/s. The elastic data at shot location $(z,x) = (0,0)m$ is shown in Figure 2c. We can see some converted waves which do not appear in the acoustic data. The FWI and MPI tomograms are shown in Figure 4b and 4c, respectively, and the corresponding velocity profiles are shown in Figure 4c. We can see that the MPI tomogram is moderately more accurate than the FWI tomogram.

Gulf of Mexico Data

The MPI method is applied to a streamer data set recorded in the Gulf of Mexico using 515 shots with a shot interval of 37.5 m, a time-sampling interval of 2 ms, a recording time of 10 s, and 480 hydrophones per shot. The hydrophone interval is 12.5 m, with the minimum and maximum source-receiver offsets of 198 m and 6 km, respectively. The $v(z)$ velocity model shown in Figure 5a is used as the initial model for multiscale FWI and MPI. The initial velocity model is discretized into 402×3008 grids with a grid spacing of 6.25 m in both directions.

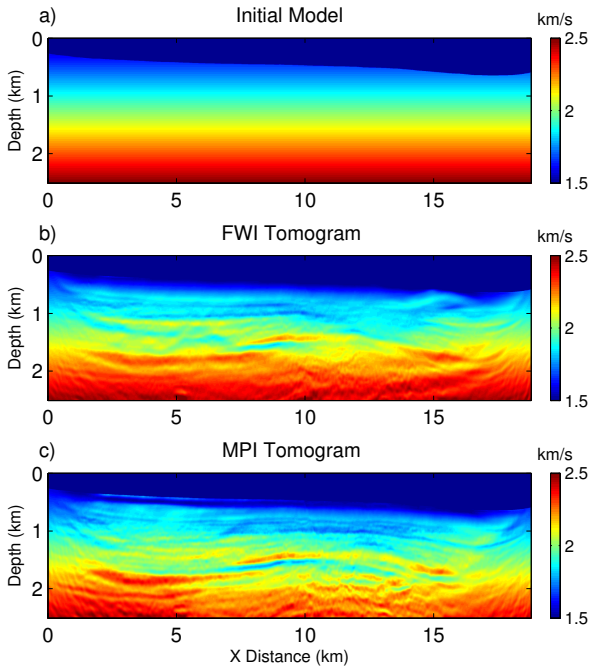

Figure 5: The a) $v(z)$ initial model, b) multiscale FWI, and c) MPI tomograms for the Gulf of Mexico data.

Figures 5b and 5c depict the FWI tomogram after 26 iterations and MPI tomogram after 52 iterations, respectively. Both the FWI and MPI tomograms have a higher resolution compared with the initial velocity model. In addition, the resolution of the MPI tomogram is slightly higher than that seen in the FWI tomogram. In order to verify the reconstructed FWI and MPI tomograms, we compare the migration images and angle domain common image gathers (ADCIGs).

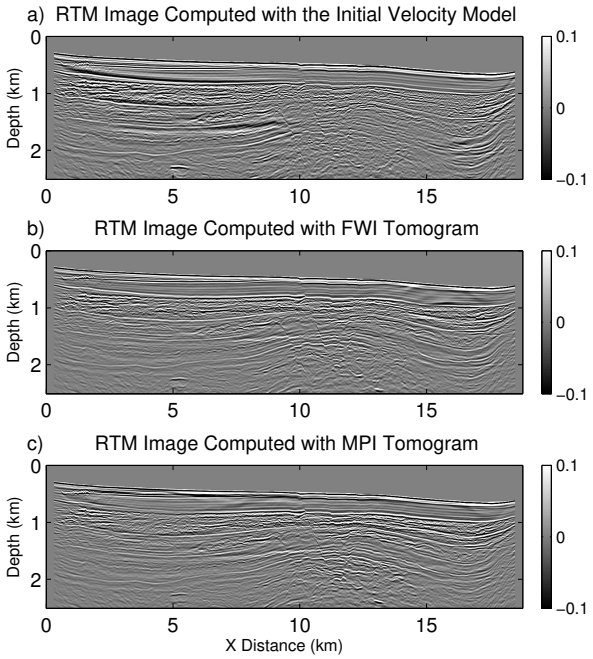

Figure 6: RTM migration images computed from a) initial velocity model, b) FWI tomogram, and c) MPI tomogram.

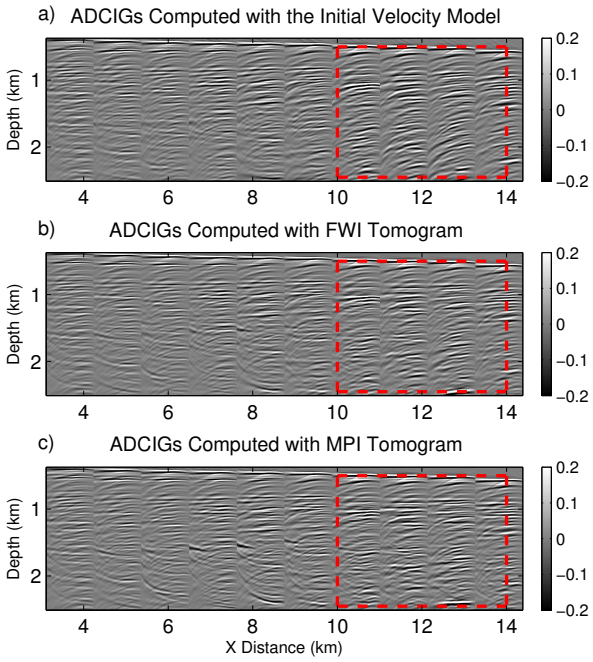

Figure 7: Angle domain common image gathers (ADCIGs) from -45° to 0° based on the a) initial model, b) FWI tomogram, and c) MPI tomogram.

The original data are migrated using reverse time migration (RTM) computed with the initial velocity model, the FWI tomogram and the MPI tomogram, and the results are shown in Figures 6a, 6b, and 6c, respectively. We see that the RTM images computed with the FWI and MPI tomograms are quite similar. The corresponding ADCIGs are shown in Figures 7a, 7b and 7c, respectively. Comparing the ADCIGs, we can see

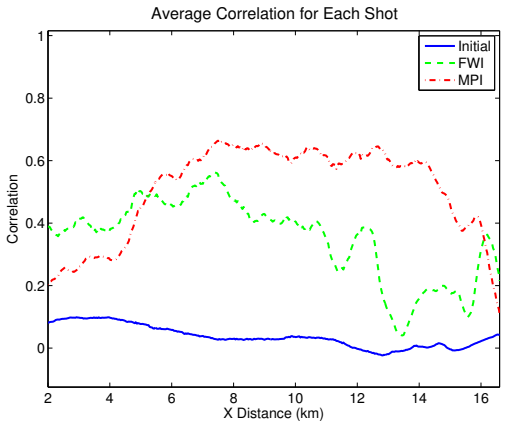

Figure 8: The average correlation, which is calculated by the correlations between the observed and predicted data, for each shot.

that the ADCIGs associated with the FWI and MPI tomograms are flatter than those from the initial velocity model. And the ADCIGs (in the red box) from MPI are slightly flatter then FWI. Figure 8 shows the data similarity between the observed and predicted data. We can find that the flattened MPI traces have a better similarity to one another than the traces obtained from the FWI tomogram.

SUMMARY AND CONCLUSIONS

The multiscale strategy temporally integrates the traces several times to produce low-boost seismograms that are used as input data for the initial iterations of MPI. Synthetic examples show that both the MIP and FWI methods can obtain similar tomograms when the initial velocity model is not far away from the true model. However, limited tests suggest that the MPI method gives a more accurate tomogram than FWI when the initial model is far from the true model. In addition, tests suggest that MPI can provide a more accurate tomogram than FWI when inverting elastic data. These examples show that MPI is more robust than FWI for inverting seismic marine data.

In the GOM marine data case, both the FWI and MPI methods successfully inverted the marine data to obtain tomograms that are more accurate than the initial velocity model. Comparing the RTM images, ADCISs and data correlations, it is found that the MPI has a slightly higher accuracy than FWI.

ACKNOWLEDGEMENTS

The research reported in this publication was supported by the King Abdullah University of Science and Technology (KAUST) in Thuwal, Saudi Arabia. We are grateful to the sponsors of the Center for Subsurface Imaging and Modeling (CSIM) Consortium for their financial support. For computer time, this research used the resources of the Supercomputing Laboratory at KAUST and the IT Research Computing Group. We thank them for providing the computational resources required for carrying out this work.

EDITED REFERENCES

Note: This reference list is a copyedited version of the reference list submitted by the author. Reference lists for the 2017 SEG Technical Program Expanded Abstracts have been copyedited so that references provided with the online metadata for each paper will achieve a high degree of linking to cited sources that appear on the Web.

REFERENCES

Alford, R., K. Kelly, and D. M. Boore, 1974, Accuracy of finite-difference modeling of the acoustic wave equation: Geophysics, **39**, 834–842, http://doi.org/10.1190/1.1440470.

Boonyasiriwat, C., P. Valasek, P. Routh, W. Cao, G. T. Schuster, and B. Macy, 2009, An efficient multiscale method for time-domain waveform tomography: Geophysics, **74**, no. 6, WCC59–WCC68, http://doi.org/10.1190/1.3151869.

Levander, A. R., 1988, Fourth-order finite-difference P-SV seismograms: Geophysics, **53**, 1425–1436, http://doi.org/10.1190/1.1442422.

Luo, Y., and G. T. Schuster, 1991, Wave-equation traveltime inversion: Geophysics, **56**, 645–653, http://doi.org/10.1190/1.1443081.

Operto, S., J. Virieux, P. Amestoy, J.-Y. LExcellent, L. Giraud, and H. B. H. Ali, 2007, 3D finite-difference frequency domain modeling of visco-acoustic wave propagation using a massively parallel direct solver: A feasibility study: Geophysics, **72**, no. 5, SM195–SM211, http://doi.org/10.1190/1.2759835.

Sirgue, L., and R. G. Pratt, 2004, Efficient waveform inversion and imaging: A strategy for selecting temporal frequencies: Geophysics, **69**, 231–248, http://doi.org/10.1190/1.1649391.

Sun, Y., and G. T. Schuster, 1993, Time-domain phase inversion: 63rd Annual International Meeting, SEG, Expanded Abstracts, 684–687, http://doi.org/10.1190/1.1822588.

Virieux, J., and S. Operto, 2009, An overview of full waveform inversion in exploration geophysics: Geophysics, **74**, no. 6, WCC1–WCC26, http://doi.org/10.1190/1.3238367.

Warner, M., and L. Guasch, 2014, Adaptive waveform inversion — FWI without cycle skipping-theory: 76th Annual International Conference and Exhibition, EAGE, Extended Abstracts, http://doi.org/10.3997/2214-4609.20141092.

Warner, M., T. Nangoo, N. Shah, A. Umpleby, and J. Morgan, 2013, Full-waveform inversion of cycle-skipped seismic data by frequency down-shifting: 83rd Annual International Meeting, SEG, Expanded Abstracts, 903–907, http://doi.org/10.1190/segam2013-1067.1